Transportation Geotechnics 56 (2026) 101766

Contents lists available at ScienceDirect

Transportation Geotechnics

journal homepage: www.elsevier.com/locate/trgeo

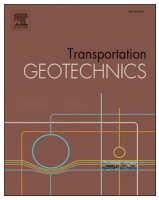

Geosynthetic-reinforced soil embankment and foundation systems subjected to reverse faulting considering soil softening behavior

Jung Chiang [a], Emerson Edwige Michel [b], Kuo-Hsin Yang [b,*]

[a] Department of Civil Engineering, National Taipei University of Technology (Taipei Tech), 1, Sec. 3, Zhongxiao E. Rd., Taipei 106, Taiwan
[b] Department of Civil Engineering, National Taiwan University (NTU), 1, Sec. 4, Roosevelt Rd., Taipei 106, Taiwan

ARTICLE INFO

Keywords:
Geosynthetic
Reverse faulting
Embankment and foundation system
Hardening soil model
NorSand model
Geocell

ABSTRACT

This study conducted a series of finite element analyses on geosynthetic-reinforced soil (GRS) embankment and foundation systems subjected to reverse fault movement. Two advanced constitutive models were considered: the hardening soil (HS) model and the NorSand (NS) model, with the latter selected to account for soil softening along the shear band under large fault displacements. The numerical models were validated by comparing their predictions with test data for reduced-scale GRS embankments with and without geocell-reinforced foundations. Subsequently, stress and displacement data were extracted to examine the performance and reinforcing mechanisms of the GRS embankment and foundation system. The development of the shear band, lateral earth pressure distribution, embankment facing deformation, and mobilization of the reinforcement tensile force were evaluated. The numerical results revealed that the NS model accurately captured the system's shear strain propagation and embankment facing deformation; this is because this model accounts for soil softening. By contrast, the HS model underestimated these responses. The numerical analyses also revealed that incorporating a geocell mattress into the foundation effectively mitigated shear band propagation from the foundation to the overlying embankment and reduced ground deformation induced by fault displacement, resulting in reduced lateral earth pressure and embankment facing deformation. In summary, geocells provide high confining pressure to infill soil, which increases its shear strength to intercept the upward propagation of shear bands and enhances bending stiffness to distribute stress over a wider influential fault zone, thereby preventing ground breakthrough in concentrated areas.

Introduction

In addition to seismic forces, ground surface deformation induced by fault movement can substantially damage structures overlying fault zones. [9,11] and [33] have identified surface hazards associated with fault movement, including distinct shear ruptures, differential settlement, and the development of tensile strains and cracks. To minimize the effects of these hazards, construction in areas near active fault zones should be avoided. Design regulations have specified certain setback distances for residential buildings to mitigate the risks of surface fault hazards. However, because of the high density of active faults in Taiwan, linear structures such as embankments, bridges, and dams are inevitably constructed across fault zones, which increases the risks associated with surface fault hazards. In these scenarios, engineering measures can be adopted to maintain the serviceability and reparability of infrastructure subjected to fault movement.

Various structural and geotechnical measures have been proposed to mitigate fault-induced ground surface deformation and thus limit foundation distortion in overlying structures. These measures can be categorized into three groups: (1) using rigid and continuous foundations to maintain rigid-body motion [3,8,18,22,23,25,38,40]; (2) embedding retaining or buffer walls to divert or absorb fault ruptures [4,19,35,37,38]; and (3) enhancing the ductility of soil layers above bedrock faults to diffuse fault ruptures [2,4,8,9,10,32,33]. Among these measures, enhancing the ductility of foundation soils by incorporating geosynthetics is considered the most effective approach for linear infrastructure. Geosynthetics can be extended over long distances to minimize the uncertainties associated with the unpredictable locations of fault-induced shear ruptures.

One notable application of the aforementioned approach is an iconic highway extension project in Taiwan. In this project, a geosynthetic-reinforced soil (GRS) embankment and foundation system was constructed at a site directly traversed by an active fault (Fig. 1a). The

* Corresponding author.
E-mail addresses: jungchiang@ntut.edu.tw (J. Chiang), d10521033@ntu.edu.tw (E.E. Michel), khyang@ntu.edu.tw (K.-H. Yang).

https://doi.org/10.1016/j.trgeo.2025.101766
Received 27 June 2025; Received in revised form 4 September 2025; Accepted 18 October 2025
Available online 24 October 2025

Nomenclature

D_{min}	minimum dilatancy (dimensionless)
e	void ratio (dimensionless)
e_c	void ratio at critical state (dimensionless)
H_f	foundation height (m)
H_w	embankment height (m)
H	plasticity hardening modulus (dimensionless)
J_{50}	reinforcement stiffness (kN/m)
L_r	reinforcement length (m)
M	stress ratio (dimensionless)
M_{tc}	stress ratio under triaxial conditions (dimensionless)
M_i	stress ratio under image conditions (dimensionless)
n	scaling factor (dimensionless)
n_G	elastic component (dimensionless)
N	volumetric coupling coefficient (dimensionless)
R_{inter}	interface reduction factor (dimensionless)
S	fault offset (m)
S_v	reinforcement vertical spacing (m)
T_{max}	maximum mobilized reinforcement tensile force (kN/m)
T_{mob}	mobilized reinforcement tensile force (kN/m)
T_{ult}	reinforcement ultimate tensile strength (kN/m)
x	distance from the left boundary (m)
γ_s	soil total shear strain (dimensionless)
Δy	wall facing displacement (m)
ε_a	soil axial strain (%)
ε_f	reinforcement tensile strain at failure (%)
ε_v	soil volumetric strain (%)
η_l	limiting stress ratio (dimensionless)
η_{max}	maximum stress ratio (dimensionless)
λ	slope of CSL (dimensionless)
ν	Poisson's ratio (dimensionless)
ϕ'	effective peak friction angle (∘)
χ_{tc}	state-dilatancy parameter (dimensionless)
ψ_0	initial state parameter (dimensionless)
ψ	state parameter (dimensionless)
τ_{max}	soil–reinforcement interface shear strength
h	elevation measured from the base of the embankment (m)
D	maximum fault displacement (m)
M_L	Richter magnitude
m	power
E_{50}^{ref}	secant modulus (kN/m^2)
E_{oed}^{ref}	tangent oedometer loading modulus (kN/m^2)
E_{ur}^{ref}	unloading–reloading modulus (kN/m^2)
c'	effective cohesion (kN/m^2)
G_{ref}	elastic shear modulus (kN/m^2)
p'	effective mean stress (kN/m^2)
q	deviatoric stress (kN/m^2)
Γ	void ratio of CSL at $p' = 1$ kN/m^2 (dimensionless)
σ'_3	confining pressure (kN/m^2)
σ_d	deviatoric stress (triaxial) (kN/m^2)
σ'_{yy}	horizontal lateral earth pressure (kN/m^2)
γ	soil unit weight (kN/m^3)

system consisted of a GRS foundation underlying a GRS embankment (Fig. 1b). The GRS foundation was adopted to enhance the ductility of the foundation soil and mitigate fault-induced angular distortion, while the GRS embankment was designed to accommodate differential settlement and maintain the stability of the highway embankment. [9,10] has demonstrated the benefits of incorporating geosynthetics into compacted earth fills to mitigate fault-induced ground deformation. Several experimental and numerical studies [15,46] have also explored the performance of GRS foundations under normal faulting conditions, demonstrating that ductile reinforced foundations can significantly reduce normal fault-induced angular distortion at the ground surface through tension membrane and shear rupture interception effects. However, [14] emphasized that reinforced foundations with planar reinforcement (e.g., geogrid) have limitations in mitigating reverse fault hazards. As reverse faulting occurs, reinforced foundations are primarily subjected to compression as the hanging wall moves toward the footwall, resulting in the insufficient mobilization of tensile forces within the planar reinforcement and limiting the contribution of the tension membrane effect.

Alternatively, a geocell foundation is introduced in this study to address this issue. Three-dimensional geocell mattresses can provide bending resistance under reverse faulting conditions. These geocell mattresses have been proven to enhance bearing capacity and constrain the lateral displacement of surrounding soil when subjected to axial loads [31,36,39,43,49]. Although the benefits of geocell mattresses are well established, the mechanical behavior of geocell foundations in mitigating ground surface deformation induced by reverse faulting remains underexplored. Furthermore, the overall performance of GRS embankments constructed over geocell foundations under reverse fault movement has yet to be examined, particularly with respect to embankment earth pressure distribution, facing displacement, and tensile force mobilization within the reinforcement.

Finite element (FE) analysis is a widely adopted and effective tool in geotechnical engineering owing to its versatility in implementing constitutive models to simulate complex soil behavior. Researchers have used the Hardening Soil (HS) model to simulate the hyperbolic and stress-dependent behavior of granular soils. However, this model may not accurately capture the post-peak strain-softening behavior observed in dense granular soils. This limitation may reduce the reliability of soil stress–strain response predictions, particularly in scenarios involving ground surface deformation and the development of shear ruptures associated with large fault displacements. To address this limitation, the NorSand (NS) model, an advanced soil constitutive model introduced by Jefferies [27], has been considered as an alternative in the present study for estimating the strain-softening behavior of dense granular soils subjected to large displacements. The NS model offers improved capabilities in capturing post-peak strain-softening behavior in granular soils, particularly in scenarios involving large ground deformation such as soil liquefaction [6,20,28,41,45]. These enhanced capabilities may contribute to a clearer understanding of shear band development and soil-geosynthetic interaction under large fault displacements.

The present study conducted a series of FE analyses to investigate the performance of GRS embankment and foundation systems subjected to reverse fault movement. Two advanced constitutive models were employed: the HS and NS models, with the latter chosen to capture strain-softening behavior along shear bands under large fault displacements. The numerical model was first validated against experimental data obtained from reduced-scale GRS embankments with and without geocell-reinforced foundations. Following validation, full-scale analyses were conducted to evaluate the system's performance and mechanical behavior under reverse faulting conditions. This study specifically focused on (1) the capability of the HS and NS models to capture the strain-softening behavior of soils under large fault displacements, (2) the reinforcing mechanisms of geocell foundations, (3) the mechanical response of the overlying GRS embankment, and (4) the design implications for GRS embankment and foundation systems against reverse fault hazards.

(a)

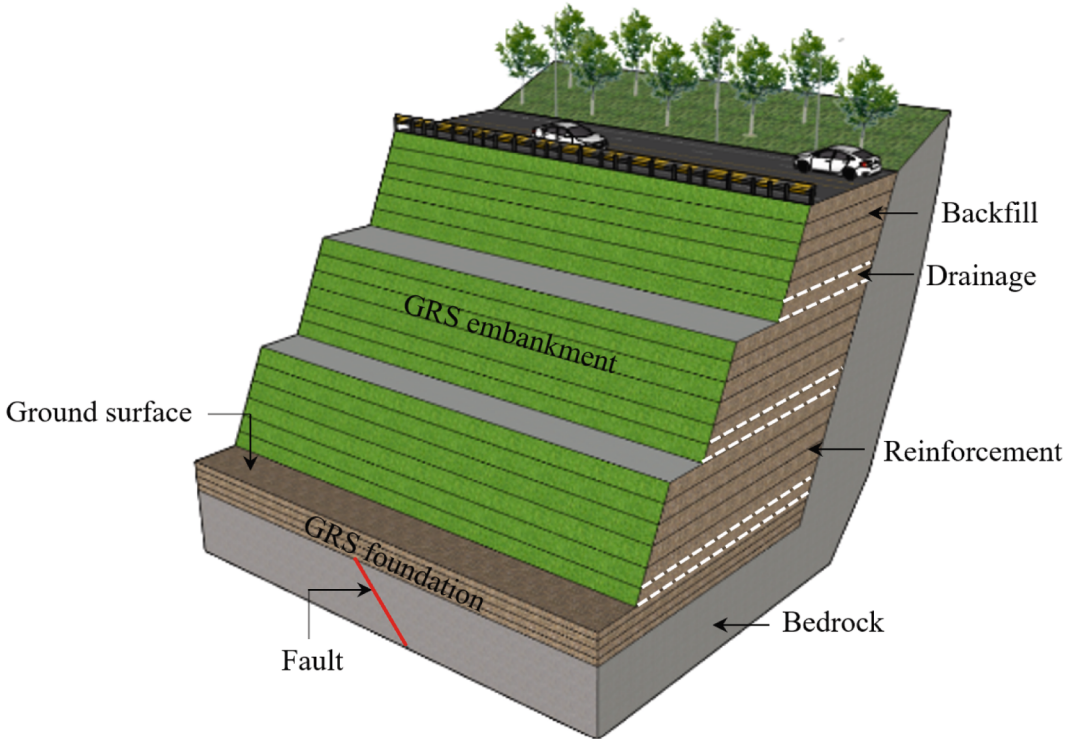

(b)

Fig. 1. GRS structures constructed in central Taiwan as a highway embankment to mitigate hazards associated with surface fault rupture: (a) photo during construction; (b) schematic illustration.

Numerical models

Three-dimensional numerical models were developed using the FE software PLAXIS [12]. Reduced- and prototype-scale numerical models were used to validate the numerical approach and assess the performance of the GRS embankment and foundation system under reverse faulting conditions, respectively. The determination of input soil parameters for the HS and NS constitutive models, reinforcement properties, and similitude requirements is presented in this section. The numerical model and boundary conditions are also described.

Input soil parameters

The input soil parameters for the HS and NS models were determined

Table 1
Input soil properties for the HS model.

Soil Properties	Values
Index property	
Unit weight, γ (kN/m^3)	15.3
Stiffness properties	
Secant modulus, E_{50}^{ref} (kN/m^2)	38,000
Tangent oedometer loading modulus, E_{oed}^{ref} (kN/m^2)	38,000
Unloading-reloading modulus, E_{ur}^{ref} (kN/m^2)	96,000
Strength properties	
Effective friction angle, ϕ′ (°)	41
Effective cohesion, c' (kN/m^2)	0
Dilation angle, ψ (°)	11
Power, m	0.5

Table 2
Input soil properties for the NS model.

Soil Properties	Values
Index property	
Unit weight, γ (kN/m^3)	15.3
Stiffness properties	
Elastic shear modulus, G_{ref} (kN/m^2)	37,000
Elastic component,n_G	0.5
Poisson's ratio, ν	0.25
Critical state ratio, M_{tc}	1.27
Volumetric coupling coefficient, N	0.35
State-dilatancy parameter, χ_{tc}	4.3
Plasticity hardening modulus, H	200
Strength properties	
Void ratio of CSL at $p' = 1$ kPa, Γ	0.91
Slope of CSL, λ	0.01
Initial state parameter, ψ_0	−0.16

through laboratory triaxial consolidated–drained (CD) compression tests conducted on uniform quartz sand that had been used in reduced-scale physical model tests [14]. As granular materials with high permeability were used in constructing the foundation for the highway extension project, all simulations were performed under drained conditions. No pore water pressure was generated during the faulting simulations, and its effect on strain-softening behavior is not evaluated in the present study. Tables 1 and 2 provide a summary of the input soil parameters for the HS and NS models, respectively. The HS model represents soil as a stress-dependent, hyperbolic, elastoplastic material and includes strength and stiffness parameters [42]. These parameters were calibrated using the SoilTest tool in PLAXIS by best fitting the stress–strain responses obtained from the triaxial compression tests. Additional details on the calibration and determination of the parameters used in the HS model are provided in the article by Chiang et al. [16].

The NS model is a work-plasticity model developed within the framework of critical state soil mechanics [5,27,30]. Although the NS model requires elaborate parameter calibration from laboratory triaxial tests and advanced theoretical knowledge compared with the HS model, it remains valuable in design practice where large deformations and strain-softening behavior are considered, such as in fault-induced ground deformation problems. This model allows for an infinite number of yield surfaces that do not necessarily intersect with the critical state line (CSL) [27,29]. The position of the yield surface is governed by the state parameter (Ψ), which approaches zero as shear strain increases. The NS model incorporates an internal cap to limit the stress ratio and prevent unrealistic stress paths. It also includes a hardening law defined by both a plastic strain parameter and the state parameter. The yield

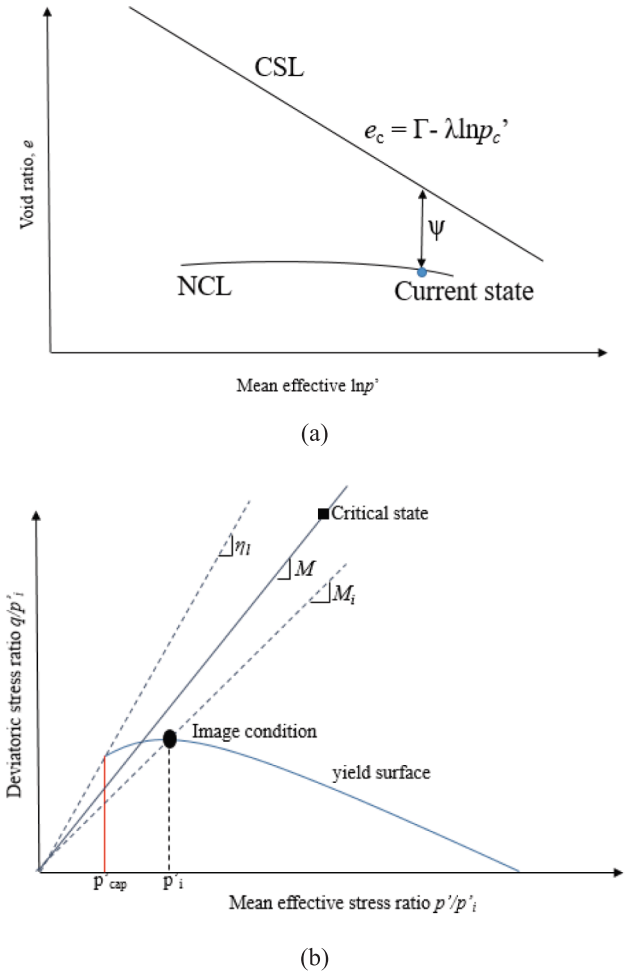

Fig. 2. NS Model: (a) definition of the state parameter; (b) description of the yield surface and its components (Adapted from Jefferies, 2015).

surface, flow rule, and hardening law collectively describe the soil response, as illustrated in Fig. 2. The major input soil parameters for the NS model were determined as follows:

Determination of CSL

The CSL is described by the following equation:

$$e_c = \Gamma - \lambda \ln(p') \quad (1)$$

where Γ is the reference void ratio on the CSL at a p' value of 1 kPa, λ is the slope of the CSL in the e-ln(p') space, and p' is the effective mean stress. Fig. 3a illustrates the changes in the void ratio of uniform quartz sand observed during triaxial tests conducted at p' values of 50, 100, and 200 kPa. The fitted line obtained at the end of the test void ratios was used to establish the equation of the CSL, which was in turn used to determine the intercept (Γ = 0.91) and slope (λ = 0.01) of the CSL.

Determination of M_{tc} and N

To determine the friction ratio in the critical state under triaxial conditions (M_{tc}), the minimum dilatancy (D_{min}) from each CD test was plotted against the corresponding maximum stress ratio (η_{max}), as displayed in Fig. 3b. In this plot, the intersection of the fitted line with the vertical axis (indicating zero dilatancy) represents the value of M_{tc} under triaxial compression conditions. The corresponding value of M_{tc} (as a model parameter) was set to 1.27. In addition, the volumetric coupling coefficient N was obtained from the slope of the fitted line, which corresponded to 1-N.

Determination of χ_{tc}

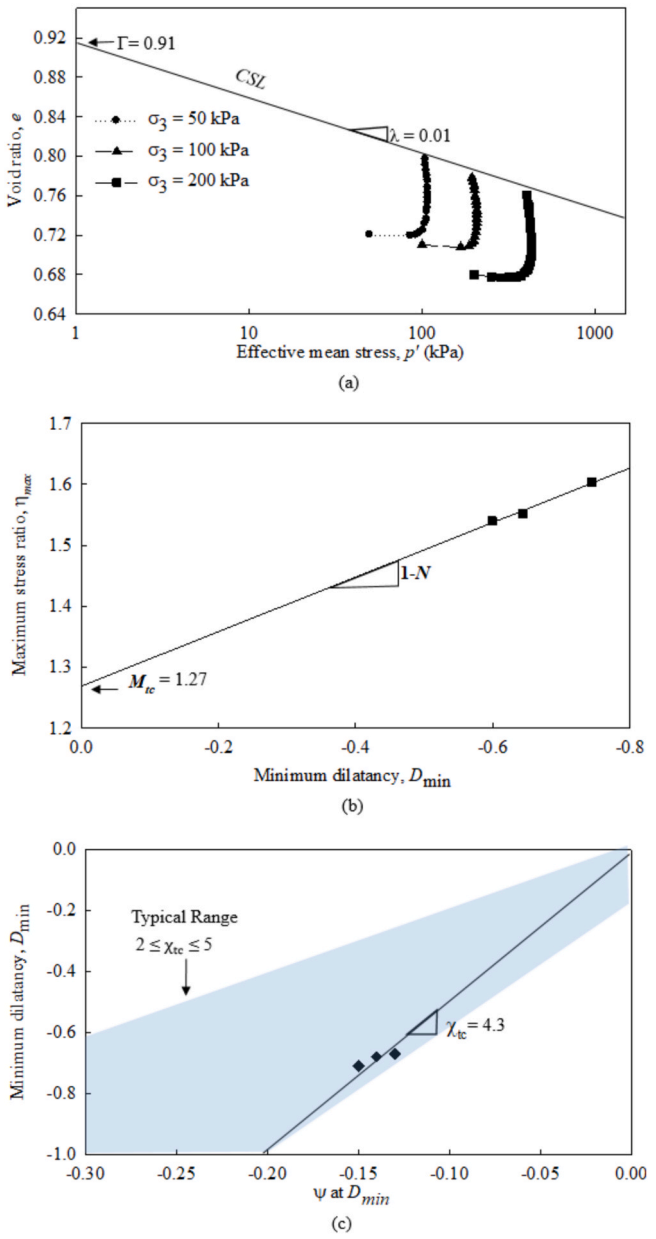

Fig. 3. Calibration for NS parameters: (a) CSL locus Γ-λ; (b) M_{tc} and N; (c) χ_{tc}.

The coefficient of maximum dilatancy (χ_{tc}) describes the soil dilatancy state in the NS model, which controls the plastic behavior of soil. To estimate χ_{tc}, the corresponding state parameter for the three applied confining pressures was plotted against D_{min} (Fig. 3c). The gradient of the obtained fitted line describes the value of χ_{tc}, which was 4.3. Other parameters, including elastic shear modulus (G_{ref}), plasticity hardening modulus (H), and Poisson's ratio (ν), were set based on recommendations provided by [17,21,28]. Furthermore, a nil phase was introduced before applying the prescribed displacement. During this phase, a plastic-type calculation with no displacement was performed to establish the initial stress state while incorporating the NS model parameters. This step was implemented to initialize the NS model parameters in accordance with the instructions given in the PLAXIS user manual. The resulting stress state corresponds to the initial condition in which the state parameter $\psi_0 = -0.16$. The negative value indicates that the initial condition of the soil material is in a dense state, which is consistent with the assumption of compacted granular foundation soil.

To validate the calibrated input parameters for both models, this study compared the stress–strain responses of the soil materials measured in the laboratory triaxial tests with those predicted by the HS and NS models, as presented in Fig. 4. Although the two models provided reasonable predictions of peak shear strength, the NS model outperformed the HS model by more accurately reproducing post-peak strain softening and volumetric expansion due to soil dilation. The coefficient of determination (R^2) between the measured and predicted stress–strain responses was 0.987 in the NS model. This strong agreement highlights the model's ability to capture the post-peak behavior, which was particularly essential for large deformations induced by reverse faulting.

Reinforcement properties

In the FE analyses, the reinforcement was modeled as a linear elastic–perfectly plastic material. Table 3 presents a summary of the reinforcement properties used in both the reduced- and prototype-scale FE models. The input values for model validation were obtained from wide-width tensile tests [1] reported by [14]. These tests were conducted on nonwoven geotextile used in the reduced-scale physical model tests, which exhibited an ultimate tensile strength (T_{ult}) of 0.7 kN/m and a tensile stiffness (J_{50}) of 5.47 kN/m in the machine direction. During the simulations, the reinforcement was manually deactivated to simulate reinforcement breakage when the mobilized tensile force reached T_{ult}. Furthermore, the geocell was modeled as a three-dimensional, honeycomb-like structure constructed from geogrid elements. This approach provides a more realistic representation of the geocell geometry and its interaction with the surrounding soil. Specifically, the confining effect and tensile behavior of the geocell are captured through interaction between soil, reinforcement (i.e., geogrid elements), and interface elements, which collectively simulate load transfer and boundary constraint mechanisms. Table 3 also presents the scaling factors and corresponding prototype values of the reinforcement properties. These factors were determined following Buckingham's π theorem [13] and have been validated in previous studies [24,44,47,48]. On the basis of similitude laws, the scaling factors for both T_{ult} and J_{50} of the reinforcement were determined as $1/n^2$, where n represents the target scaling ratio. The n value was set to 15 to ensure consistency with the actual tensile strength properties of the reinforcement and to provide a reasonable response for the prototype GRS system.

The soil–reinforcement interaction was simulated using linear elastic–perfectly plastic interface elements. The soil–reinforcement interface shear strength (τ_{max}) was defined using the Mohr–Coulomb failure criterion and is expressed as follows:

$$\tau_{max} = R_{inter} \times \sigma_n tan\phi' \quad (2)$$

where R_{inter} is the interface reduction coefficient, σ_n is the normal stress acting on the soil–reinforcement interface, and ϕ' is the soil effective friction angle. Reinforcement pullout is initiated when the mobilized shear stress at the soil–geotextile interface reaches or exceeds τ_{max}. In this study, R_{inter} was set to 0.9 for the sand–geotextile interface, consistent with the value reported by Chiang et al. [16].

Numerical models and boundary conditions

Fig. 5 presents the numerical models of the GRS embankment and foundation system. The heights of the reduced-scale GRS embankment (H_w) and foundation (H_f) were 12 and 20 cm, respectively, and their lengths were both 100 cm (Fig. 5a). As highlighted in previous studies [16,23], the mesh size of numerical models significantly influences the thickness of fault-induced shear bands. Thicker shear bands were observed when a coarse mesh was adopted, whereas relatively narrow and more localized shear bands were obtained with a finer mesh. Accordingly, a fine mesh was employed in the critical fault zone to better capture the characteristics of shear band development induced by

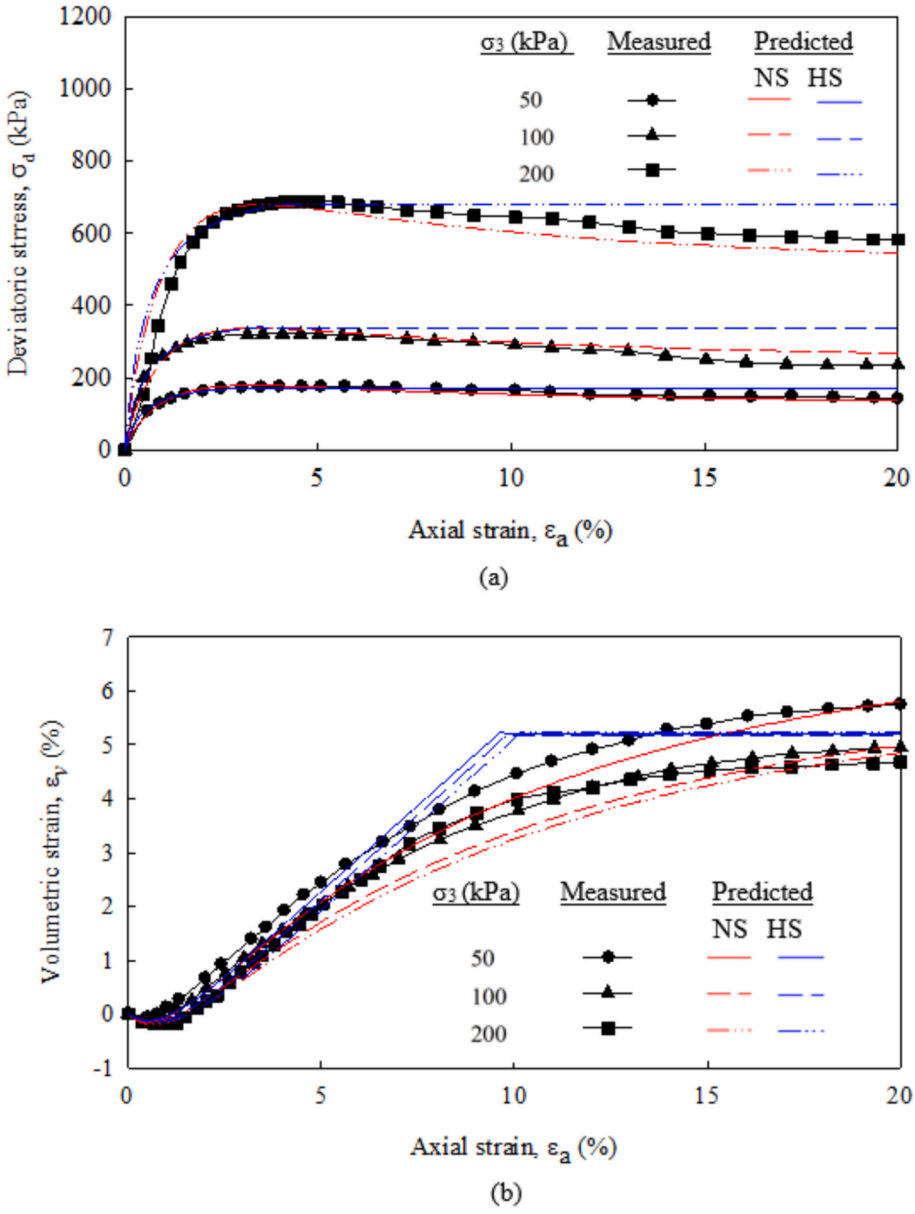

Fig. 4. Calibration of soil parameters using triaxial test results: (a) deviatoric stress vs. axial strain; (b) volumetric strain vs. axial strain.

Table 3
Input reinforcement and soil-reinforcement interface properties.

Properties	Scaling factor [a]	Values	
		Reduced scale [b]	Prototype
Reinforcement			
Ultimate tensile strength, T_{ult} (kN/m)[MD]	$1/n^2$	0.70	150
Ultimate tensile strength, T_{ult} (kN/m)[CMD]	$1/n^2$	0.245	60
Stiffness, J_{50} (kN/m)[MD]	$1/n^2$	5.47	1231
Stiffness, J_{50} (kN/m)[CMD]	$1/n^2$	0.45	100
Failure strain, ε_f (%)[MD]	1	32.4	32.4
Failure strain, ε_f (%)[CMD]	1	87.4	87.4
Soil-Reinforcement Interface			
Interface reduction factor, R_{inter}	1	0.9	0.9

[a] target scaling factor $n = 15$.
[b] used in model validation
[MD] machine direction
[CMD] cross-machine direction

reverse-fault movement. After model validation, prototype-scale models (Fig. 5b) were established to examine the mechanical behavior of the system under reverse fault movement conditions. Both the prototype GRS embankment and foundation had a height of 3 m and a length of 15 m. The reinforcement layout of the prototype GRS embankment complied with a conventional vertical spacing of $S_v = 0.5$ m and a reinforcement length of $L_r = 0.7 \cdot H_w = 2.1$ m. In geocell foundations, the geocell mattress was positioned at a depth of $1/3\ H_f$ and extended across the entire foundation, with prototype dimensions of 20 × 20 × 30 cm (length × width × height) for single cellular units (Fig. 5c).

In the initial phase, standard fixities were applied to the model boundaries. The displacement in the x-direction at the left and right boundaries was constrained (i.e., $u_x = 0$, $u_y \neq 0$, $u_z \neq 0$), while the bottom boundary was fully fixed (i.e., $u_x = 0, u_y = 0, u_z = 0$). The top and facing of the embankment were left free to deform under fault movement. These boundary conditions ensured that the numerical model could properly simulate the deformation behavior of the GRS embankment and foundation system subjected to fault movement. A prescribed displacement was then applied to the bottom and right boundaries of the

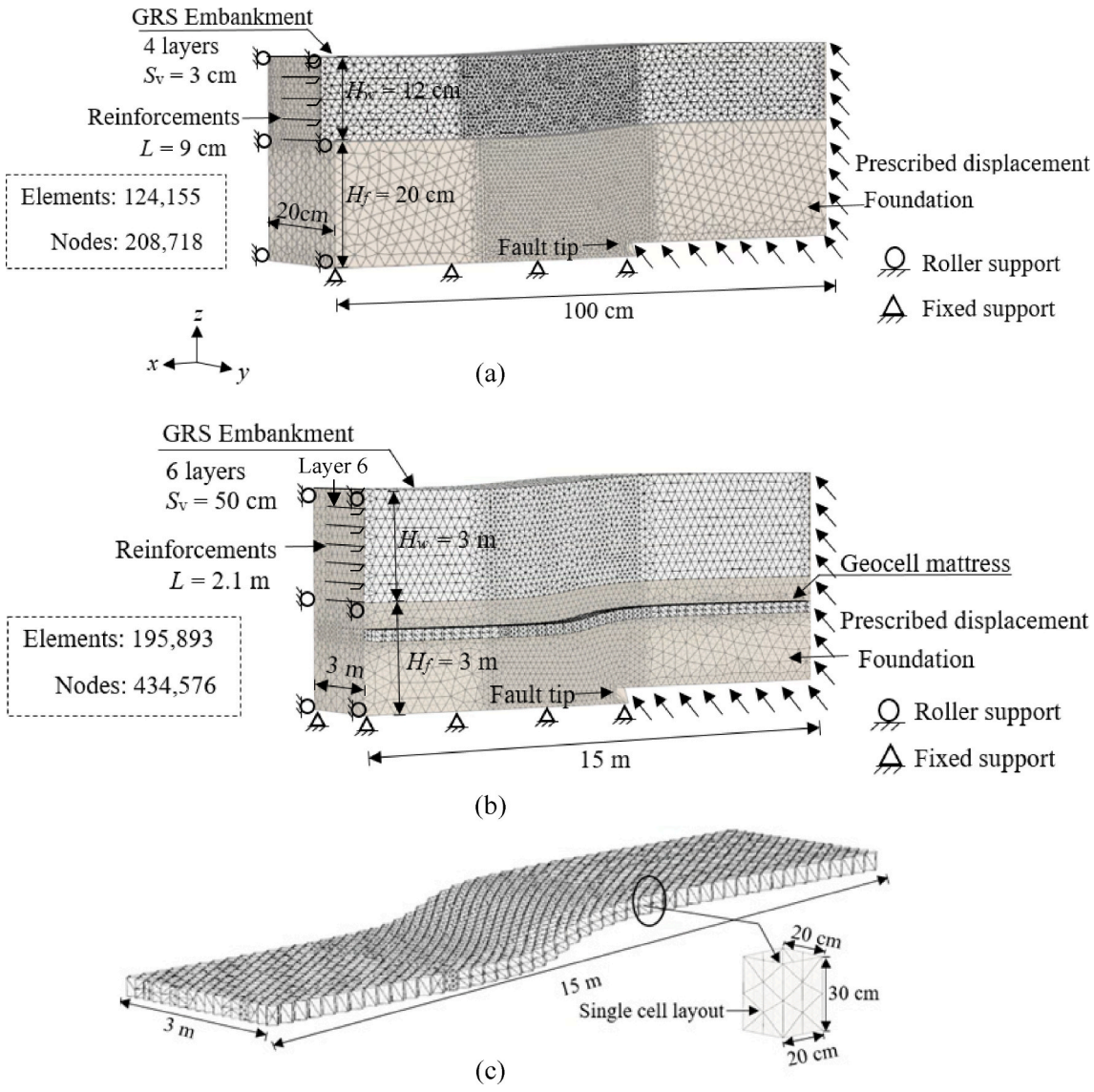

Fig. 5. Numerical models of the embankment-foundation system: (a) unreinforced case (model test); (b) reinforced case (full scale); (c) close view of geocell mattress.

hanging wall to simulate 60° dip reverse fault movement. The displacement fault movement was applied incrementally, with the maximum vertical displacement at the base of the hanging wall (S) set to 4.5 cm for model validation, corresponding to an S/H_f value of 22.5%, where S/H_f is the ratio of vertical displacement to foundation height. In the prototype simulation, the maximum vertical displacement was set to correspond to an S/H_f value of 25% (i.e., $S = 0.75$ m, and $H_f = 3$ m). The maximum vertical displacement was determined based on the fault offset associated with strong earthquakes, as defined by the U.S. Geological Survey [7], and is further discussed in section 4.3.

To ensure numerical stability, specific settings were implemented for the NS model simulations. Smaller load steps were adopted, while the tolerance and other numerical parameters remained at their default values. The maximum load fraction per step was set to a low value (0.1–0.5), and gradual error reduction was enabled to enhance numerical stability. Furthermore, the maximum fault offset was applied in phases with small increments, and the mesh was updated at each phase to account for large deformations.

Model validation and comparison

Model validation was carried out by comparing the numerical predictions with experimental measurements from physical model tests conducted by Chiang et al. [14]. The numerical models were validated by comparing shear band development in unreinforced and geocell-reinforced foundations and embankment facing displacement (Δy) induced by reverse fault movement. The HS and NS models were also compared to determine their accuracy and reliability. In addition, stress paths at selected locations were analyzed to evaluate the stress states associated with each model during shear band development.

Comparison of shear band development and facing displacement

Fig. 6 presents a comparison of the measured and predicted shear band development in the unreinforced and geocell-reinforced foundations at various fault offsets. The measured shear strain contours were obtained using particle image velocimetry (PIV) analysis in the physical model tests. The comparative results indicated that the NS model exhibits superior capability in capturing the bending behavior of the fault-induced shear band in the unreinforced foundation. In the NS model, the

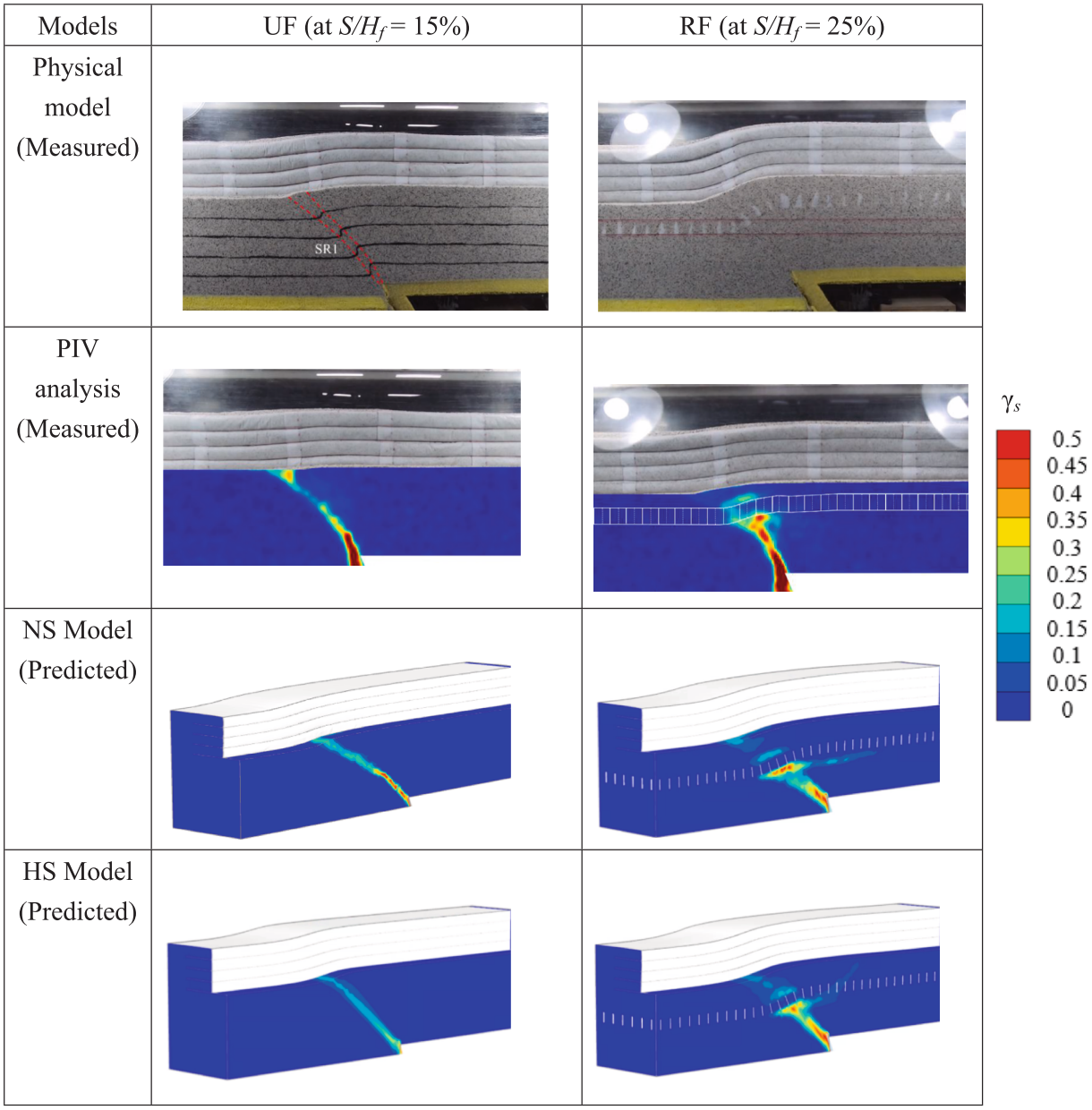

Fig. 6. Experimental and numerical results of shear band propagation within the embankment-foundation system.

dip angle of the shear band decreased gradually with increasing fault displacement; by contrast, in the HS model, the shear band exhibited a constant dip angle. The bending of the shear band in the unreinforced foundation (i.e., free-field condition) in the NS model is consistent with the results of previous physical model tests and numerical simulations [34] and with field observations [9,10]. Nonetheless, the HS and NS models demonstrated high accuracy in capturing shear band development in the geocell foundations. Notably, the displacement on the top surface of the embankment near the left and right boundaries of the numerical model was negligible, and the fault-induced shear rupture did not reach the boundaries, indicating that the boundary conditions has minor effects on the stress and deformation distributions caused by reverse fault movement.

Fig. 7 presents a comparison of the predicted and measured embankment facing displacements over the unreinforced and geocell-reinforced foundations at various fault offsets. The vertical axis indicates the normalized embankment height h/H_w, where h is the elevation measured from the base of the embankment. The results revealed that the NS model predictions were in good agreement with the physical model test results. However, the HS model substantially underestimated the embankment facing displacements, particularly at large fault offsets (i.e., S/H_f = 22.5%). Fig. 8 shows a quantitative comparison between the measured and predicted facing displacements using error metrics R^2 and the Root Mean Square Error (RMSE). The NS model achieved an RMSE of 0.74, whereas the HS model yielded a substantially higher value of 2.71, indicating that the NS model provides a closer fit to the observed data and reduces prediction error by approximately 73% relative to the HS model. Comparative R^2 results under both unreinforced and geocell-reinforced foundations further support the superiority of the NS model. From an engineering perspective, this enhanced predictive capability is particularly significant, as it allows for more reliable estimation of post-peak soil–structure interaction and large-strain deformation behavior. In summary, although the HS model can qualitatively capture shear band development in geocell foundations, its ability to predict embankment facing displacement induced by reverse faulting remains limited.

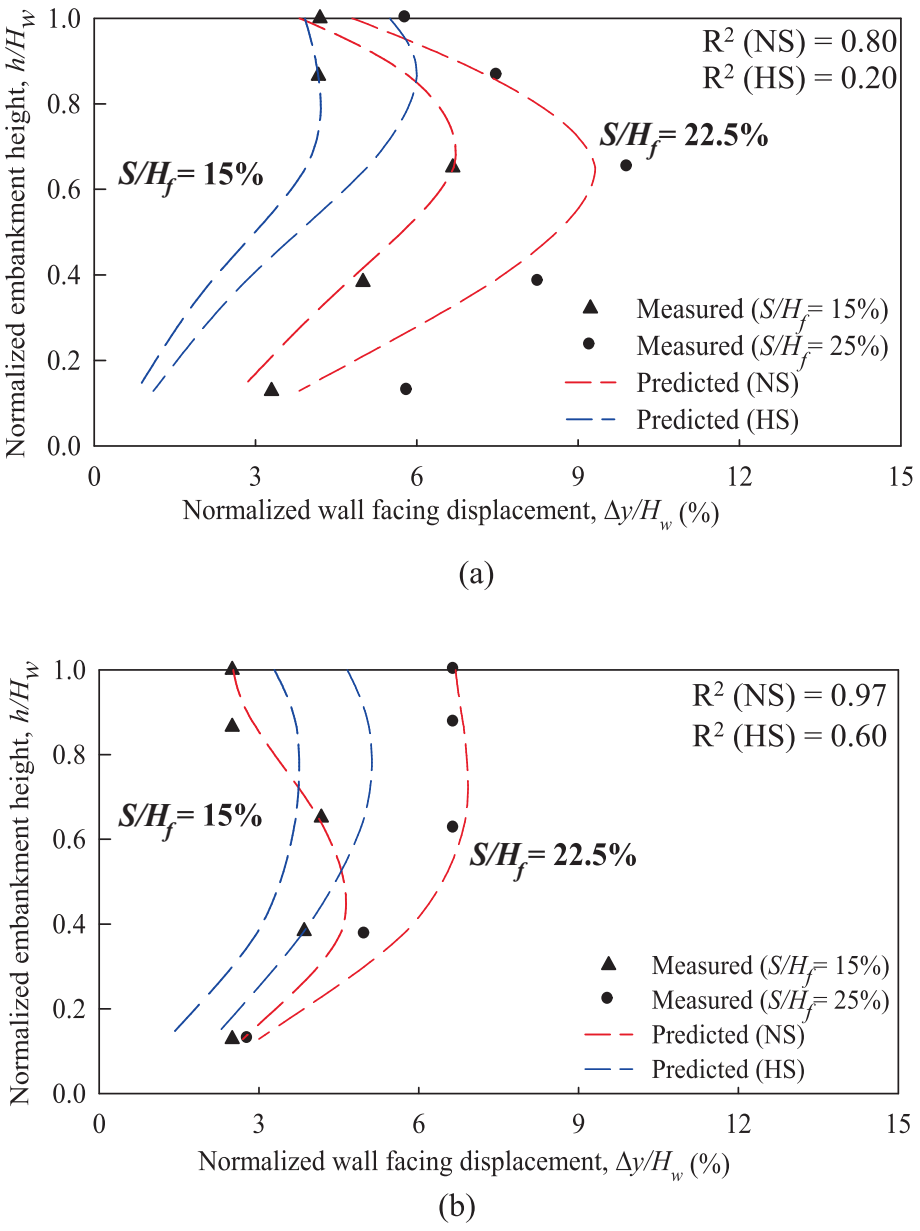

Fig. 7. Validation for the embankment facing displacement profile: (a) unreinforced embankment-foundation system; (b) reinforced embankment-foundation system.

Comparison of stress paths

Fig. 9 illustrates the stress paths of two specific points along the shear band, namely Point A (near the outcrop) and Point B (near the fault tip), predicted by the HS and NS models. The stress paths indicate that the soil material experienced a lateral compression (LC) loading state under reverse faulting conditions, as evidenced by the decrease in vertical stress and increase in horizontal stress. The deviatoric stress (q) became negative while the effective mean stress (p') increased, indicating that principal stress rotation occurred as the fault offset increased. Furthermore, the HS model exhibits a gradual progression toward the K_f −line and ductile failure, whereas the NS model shows brittle failure; both are consistent with the stress–strain response observed in the triaxial compression tests. Strain softening is observed in the NS model as the stress path reaches the K_f −line (at S/H_f = 3%), at which point the loading state transitions from LC to lateral extension (LE). The change in stress path from LC to LE implies a transition in the principal stress state, leading to reduced confinement and increased lateral displacement of the soil mass along the shear band. This transition highlights two beneficial effects of reinforcement by providing tensile resistance: restraining lateral displacement and enhancing confinement (which increases the shear strength of the soil), particularly under large fault displacements. Overall, the strain-softening behavior captured by the NS model can facilitate an accurate simulation of the post-peak response of GRS embankment and foundation systems subjected to large fault offsets.

Mechanical behavior of embankment and foundation systems

The mechanical behavior of the GRS embankment and foundation system subjected to reverse fault movement is investigated through full-scale FE analyses. The reinforcing mechanisms of the geocell foundation and the performance of the GRS embankment overlying unreinforced and geocell-reinforced foundations were evaluated. To simplify the discussion, the unreinforced and geocell-reinforced foundation cases herein are referred to as UF and RF, respectively. Following the model

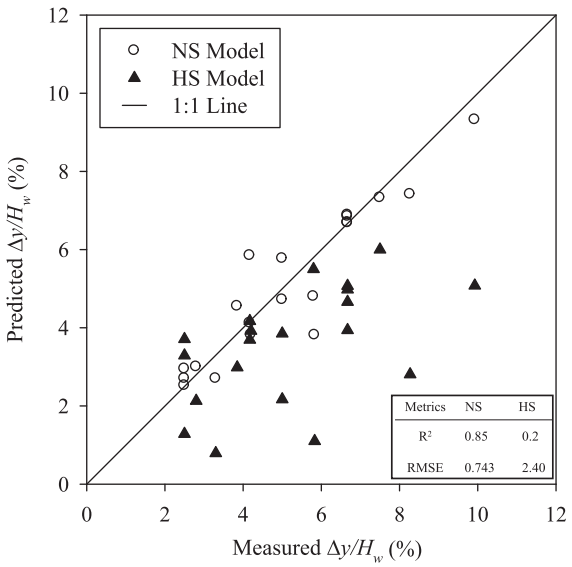

Fig. 8. A quantitative comparison between the measured and predicted facing displacements using error metrics R^2 and RMSE.

validation, the NS model is adopted in the full-scale FE analyses to assess the mechanical behaviors of the GRS embankment–foundation system subjected to reverse fault movement.

Reinforcing mechanism of the geocell foundation

Fig. 10 presents the propagation of fault-induced shear bands in the GRS embankment and foundation system in the UF and RF cases at various fault offsets. In the UF case, the shear band passed through the unreinforced foundation and extended upward to the top of the embankment. By contrast, in the RF case, the propagation of the shear band was primarily intercepted by the geocell mattress. This three-dimensional geocell mattress provided bending stiffness against the compressive forces induced by reverse faulting, dissipating the imposed stresses and thereby reducing the magnitude transmitted to the embankment. No stress concentration was observed at the top of the embankment in the RF case.

Fig. 11 depicts the variation of accumulated shear strain in the GRS embankment and foundation system at three critical locations: Points A, B, and C. Point A was located within the embankment, whereas Points B and C were positioned above and below the geocell mattress, respectively (Fig. 10). In the RF case, shear strain was considerably concentrated at Point C, but the shear strain levels were significantly reduced at Points A and B, indicating that the fault-induced shear band was intercepted by the geocell mattress. In the UF case, the shear strain levels decreased gradually as the distance from the fault tip to the recording points increased.

Figs. 12 and 13 present the distribution of horizontal stress σ'_{yy} within the geocell foundation and the corresponding σ'_{yy} profiles with respect to foundation height for both cases, respectively. The numerical results revealed that the value of σ'_{yy} within the geocell mattress increased substantially with the fault offsets. This increase in σ'_{yy} can be attributed to the additional confinement provided by the geocell units to the infill material, which enhanced the shear strength of the soil and contributed to the interception of the shear band.

Mechanical response of embankments

To assess the influence of reverse fault movement on embankment stability, fault-induced lateral earth pressure distribution, facing displacement, and reinforcement tensile force mobilization were analyzed. The mechanical responses of the embankment under reverse faulting conditions, along with the interaction between the embankment and the foundations, are discussed in the following sections.

Lateral earth pressure distribution

Fig. 14 illustrates the contours of lateral earth pressure (σ'_{yy}) within the retained zone of the embankment for the UF and RF cases at various fault offsets. Fig. 15 presents the profiles of σ'_{yy} with normalized embankment height for the UR and RF cases at various fault offsets. The profiles of the initial σ'_{yy} (i.e., lateral earth pressure at rest) and the theoretical Rankine active earth pressure are also presented in Fig. 15 for reference. The numerical results revealed that the values of σ'_{yy} within the retained zone increased with the fault offsets, with the maximum values observed primarily at one-third of the embankment height (i.e., $h/H_f \approx 0.33$). At an S/H_f value of 25%, the maximum values of σ'_{yy} predicted for the UF and RF cases were 42.9 and 27.9 kPa, respectively. The results indicated a notable decrease in the maximum value of σ'_{yy} within the retained zone for the RF case, indicating that the embankment experienced lower horizontal thrust, which in turn enhanced its external stability against sliding and overturning when subjected to reverse faulting. Notably, the location of the maximum fault-induced lateral earth pressure within the retained zone of the embankment is a specific trend obtained from the present FE analyses, rather than a general or theoretical observation. As reverse fault movement occurs, stress concentration develops at approximately one-third of the embankment height due to the formation of the fault-induced shear band, resulting in pronounced lateral earth pressure at this depth.

Facing displacement

Fig. 16 presents the contours of normalized embankment facing displacement ($\Delta y/H_w$) for the UF and RF cases at various fault offsets. The results indicated that the embankment facing displacement on the footwall side increased significantly with reverse fault offsets, whereas a negligible displacement was observed on the hanging wall side. Fig. 17 illustrates the profiles of $\Delta y/H_w$ with normalized embankment heights for the UF and RF cases at various fault offsets. The results revealed that the maximum facing displacement occurred at the topmost reinforcement layer (i.e., Layer 6) because of the relatively low pullout resistance of the reinforcement. Furthermore, Δy decreased notably with the inclusion of the geocell mattress, particularly at large fault offsets. At an S/H_f value of 25%, the maximum $\Delta y/H_w$ values predicted for the UF and RF cases were 10.4% and 8.5%, respectively, indicating an 18% reduction in the RF case. As outlined in the previous section, the geocell mattress intercepted the fault-induced shear band and dissipated the imposed stress transmitted to the embankment by providing bending resistance, thereby mitigating Δy induced by reverse fault movement.

Reinforcement tensile force mobilization

Fig. 18 displays the contours of mobilized tensile forces (T_{mob}) in the embankment's reinforcement layers in the transverse direction (i.e., y-axis) for the UF and RF cases at various fault offsets. Overall, T_{mob} increased with the reverse fault offsets, with pronounced mobilization occurring at the location intersecting with the fault-induced shear band (Figs. 10 and 18). Fig. 19 presents the profiles of the maximum mobilized tensile forces (T_{max}) with normalized embankment heights for the UF and RF cases at various fault offsets. The numerical results indicated that the peak T_{max} occurred in the reinforcement layer positioned at one-third of the embankment height (i.e., Layer 3 at $h/H_w \approx 0.33$). At an S/H_f value of 25%, the predicted T_{max} values in Layer 3 for the UF and RF cases were 11.50 and 10.14 kN/m, respectively. The slight reduction in T_{max} in the RF case can be attributed to the geocell mattress, which intercepted the propagation of the shear band, thereby reducing the fault-induced lateral earth pressure and the associated mobilization of tensile forces. Notably, reinforcement breakage did not occur in either case, indicating that the GRS embankment had sufficient tensile capacity to withstand large fault displacements.

Figs. 20 and 21 display the contours and distributions of T_{mob}, respectively, in the embankment reinforcement layers in the

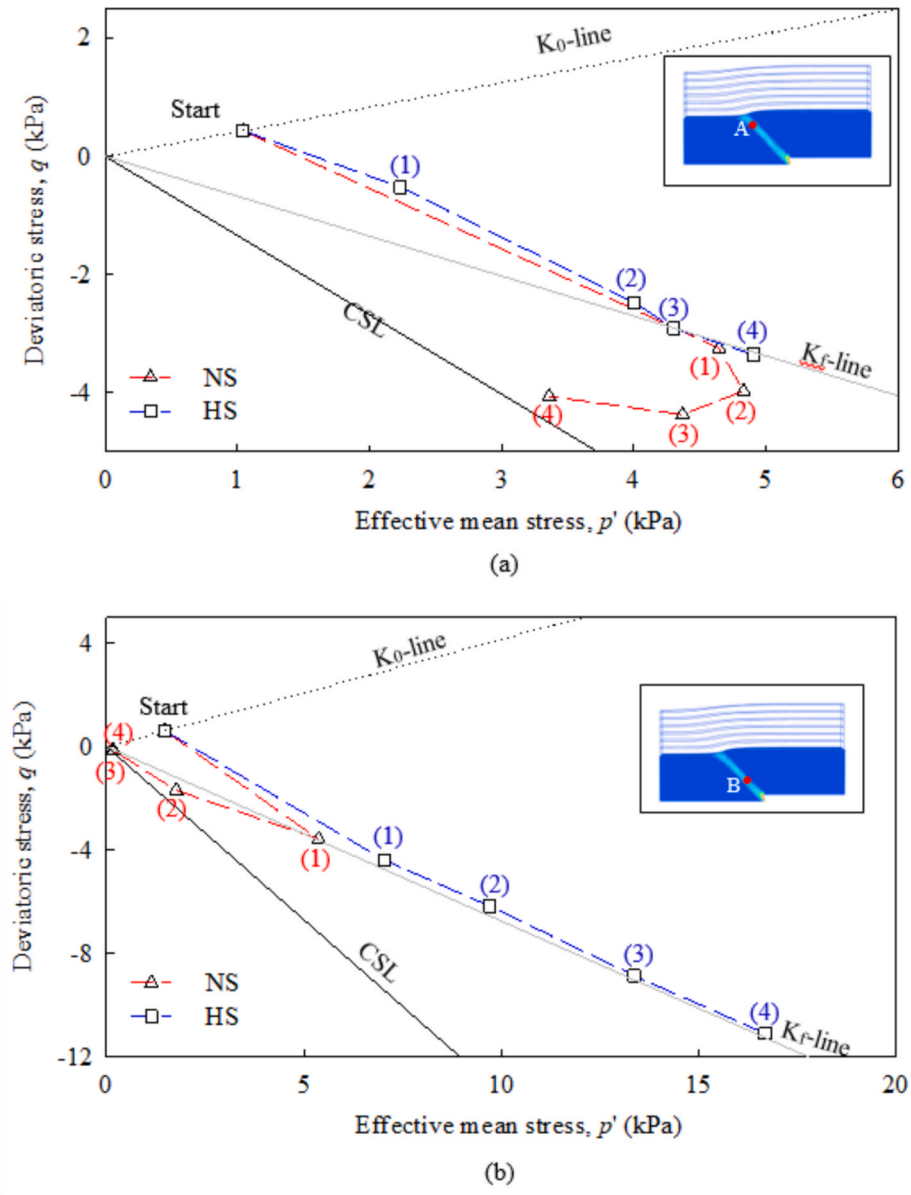

Fig. 9. Comparison of stress paths between the NS and HS models during faulting: (a) stress point A; (b) stress point B, at S/H_f of (1) 3%, (2) 7.5%, (3) 15%, and (4) 22.5%.

longitudinal direction (i.e., *x*-axis) for the UF and RF cases at various fault offsets. High values of T_{mob} were observed in the uppermost embankment reinforcement layer (i.e., Layer 6) on the hanging wall side. As reverse fault offsets occurred, a tensile zone was induced in the embankment on the hanging wall side because of the lateral movement of the soil mass toward the footwall. The tensile zone led to the concentration of T_{mob} in the upper reinforcement layers along the longitudinal direction. Notably, the geocell mattress had a limited influence on the mobilization of reinforcement tensile forces in the longitudinal direction. Specifically, the geocell mattress functioned to intercept the fault-induced shear band and reduce the stress transmitted to the embankment. By contrast, the reinforcement layer in the GRS embankment functioned to maintain embankment stability and accommodate fault-induced lateral earth pressure by providing tensile capacity and pullout resistance.

Design implications

The United States Geological Survey proposed a regression equation for estimating maximum fault displacement as a function of earthquake magnitude [7]:

$$\log D = 0.57M_L - 3.39 \tag{3}$$

where D is the maximum fault displacement (in feet) and M_L is the Richter magnitude. The maximum fault offset considered in the present full-scale FE analyses was 0.75 m (i.e., $S/H_f = 25\%$, with $H_f = 3$ m), which is equivalent to $M_L = 6.6$. According to the United States Geological Survey's earthquake classification system, earthquakes with a Richter magnitude M_L of ≥ 6.0 are categorized as strong earthquakes. Fig. 22 presents the envelopes of maximum mobilized tensile forces in the reinforcement layers of the embankment at the critical cross-section where the maximum facing displacement occurred. These envelopes were determined by connecting the peak T_{mob} for each reinforcement layer at the final fault offset stage (i.e, $S/H_f = 25\%$) for both unreinforced and geocell-reinforced foundations. In the UF case, the envelope of maximum mobilized tensile forces was close to the theoretical Rankine active failure plane, indicating a potential risk of embankment instability during strong earthquakes. By contrast, in the RF case, the

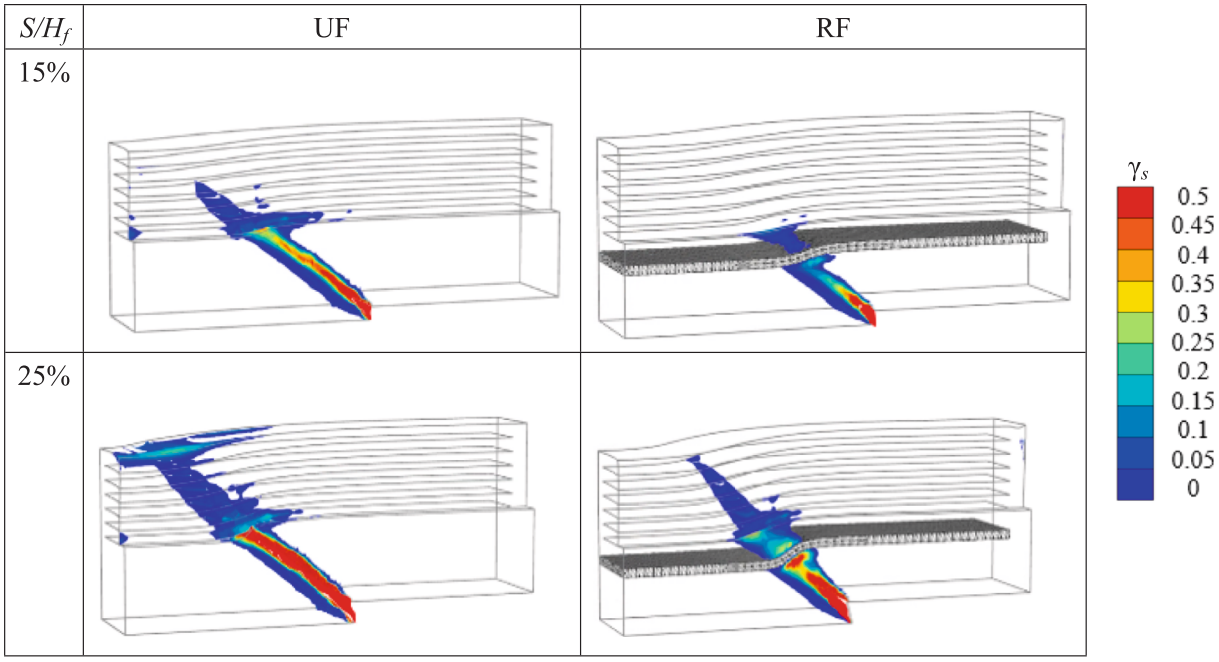

Fig. 10. Development of shear band within the embankment and foundation system.

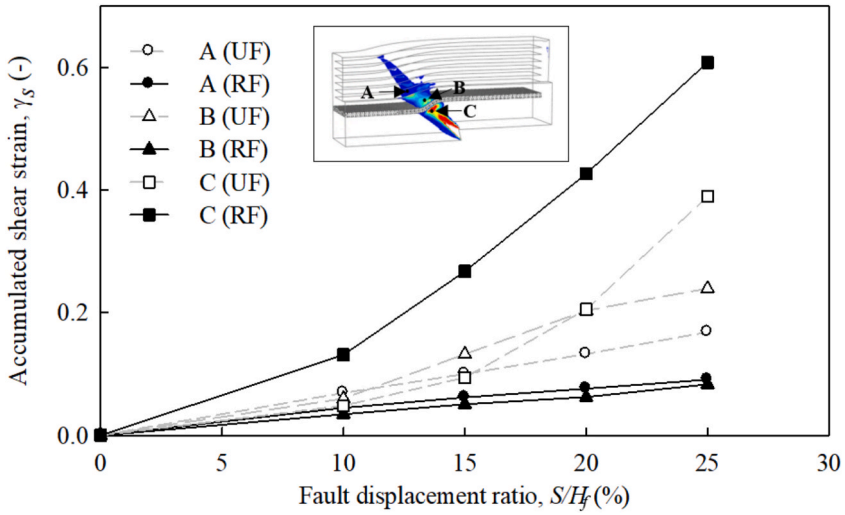

Fig. 11. Accumulated shear strain (Point A: within embankment; Point B: near outcrop; Point C: below geocell mattress).

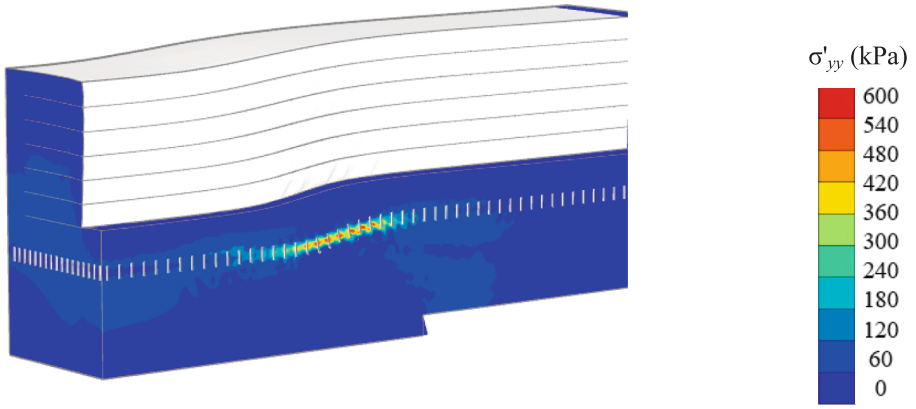

Fig. 12. Confining stress increase within geocell mattress (S/H_f = 15%).

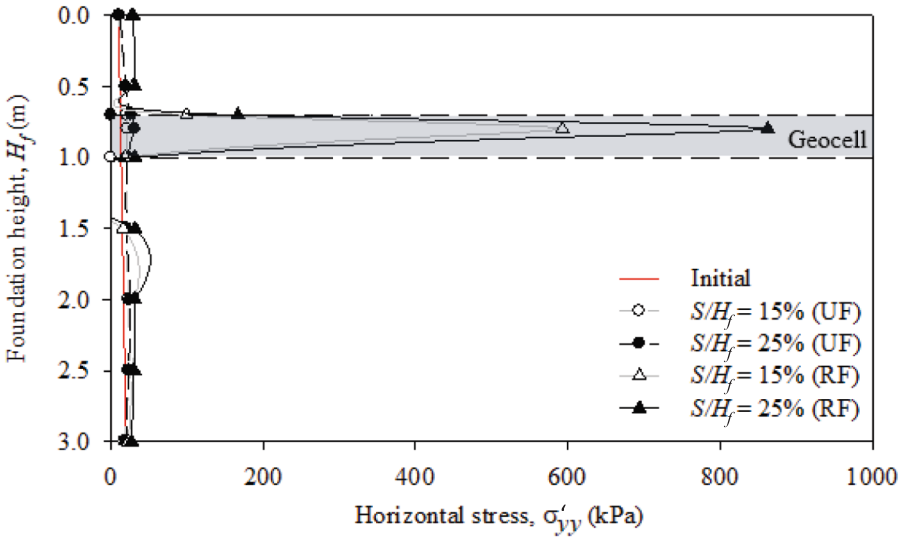

Fig. 13. Horizontal stress distribution profile within foundation at the shear band location.

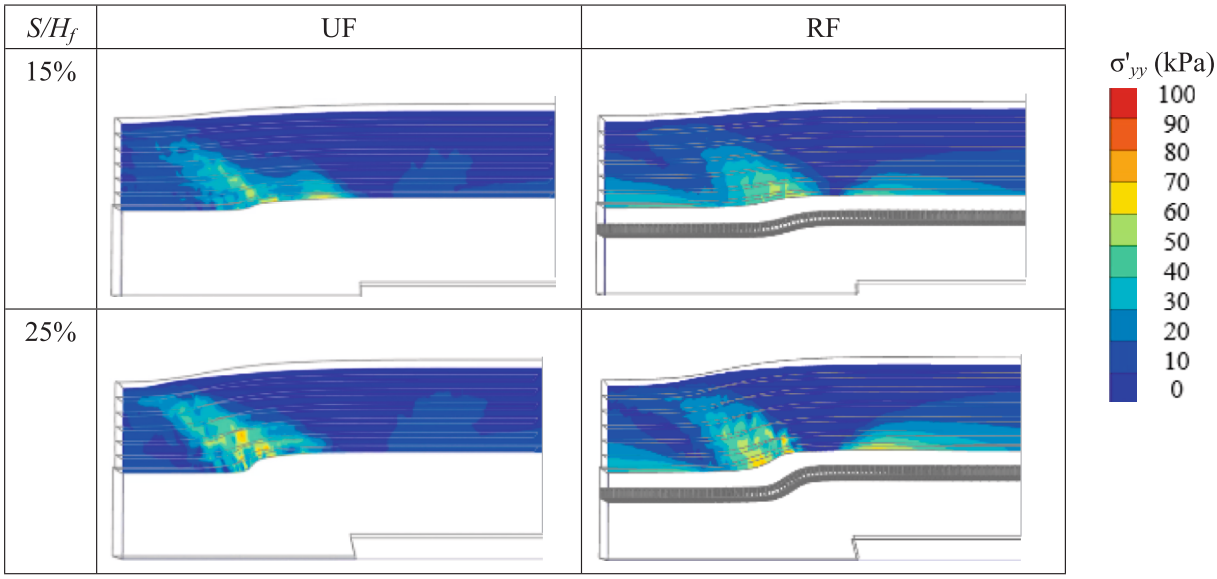

Fig. 14. Contours of lateral earth pressure within the retained zone of the embankment.

envelope of T_{max} was displaced away from the failure plane, indicating an increase in effective reinforcement length and embankment stability.

Furthermore, the ranges of maximum $\Delta y/H_w$ corresponding to the serviceability and limit states of GRS walls were determined based on centrifuge tests conducted by Hung et al. [26]. The results showed that GRS walls remained in the serviceability state when the maximum $\Delta y/H_w$ ranged from 1.5% to 3.5%, whereas the limit state occurred when the maximum $\Delta y/H_w$ ranged from 8% to 12%. As illustrated in Fig. 17, the maximum $\Delta y/H_w$ values of the embankment for the UF and RF cases fell within the range of the limit state at $S/H_f = 25\%$. These findings suggest that embankments may undergo significant localized deformation during strong earthquakes, although structural collapse may not occur. When the geocell reinforcement was applied, the maximum $\Delta y/H_w$ decreased to a value that approximated the lower bound of the limit state (i.e., $\Delta y/H_w = 8\%$ at $S/H_f = 25\%$), indicating improved embankment stability at large fault offsets. Although this value still exceeds the range for serviceability state, the associated localized deformation can be readily repaired after an earthquake to restore the serviceability of highway embankments.

In summary, geocell mattresses not only enhance embankment stability and reduce facing displacement, but also improve the bearing capacity of the underlying foundation soil. Moreover, GRS embankment–foundation systems are generally more cost-effective than rigid retaining structures with deep foundations, provided that uniform compaction within the geocell units is ensured. Therefore, a wrapped-around GRS embankment overlying a geocell foundation is recommended as an effective system for mitigating surface fault hazards associated with reverse faulting.

Conclusions

This study conducted a series of FE analyses to investigate the performance of GRS embankment and foundation systems subjected to reverse fault movement; the study considered two foundation cases: UF and RF cases. The study applied the HS and NS constitutive models, with the NS model selected to capture strain-softening behavior under large

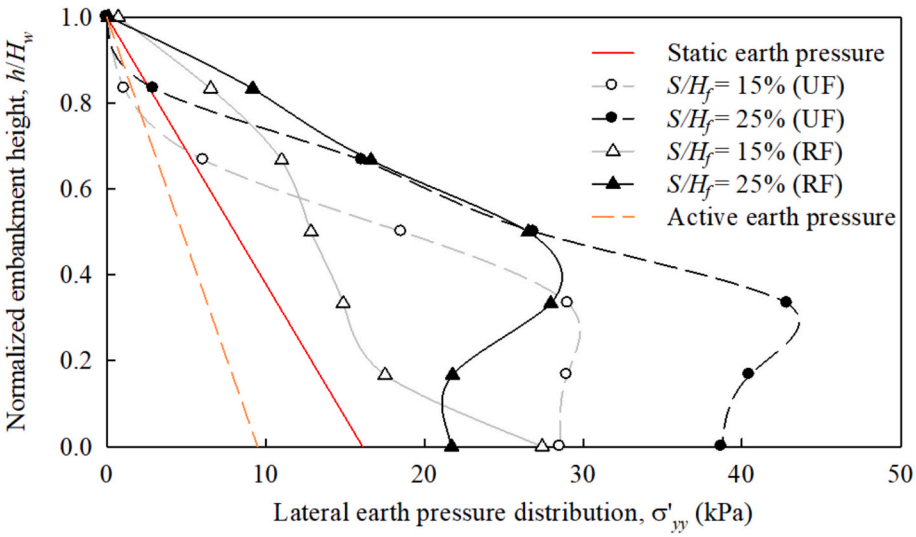

Fig. 15. Profiles of σ'_{yy} with normalized embankment height.

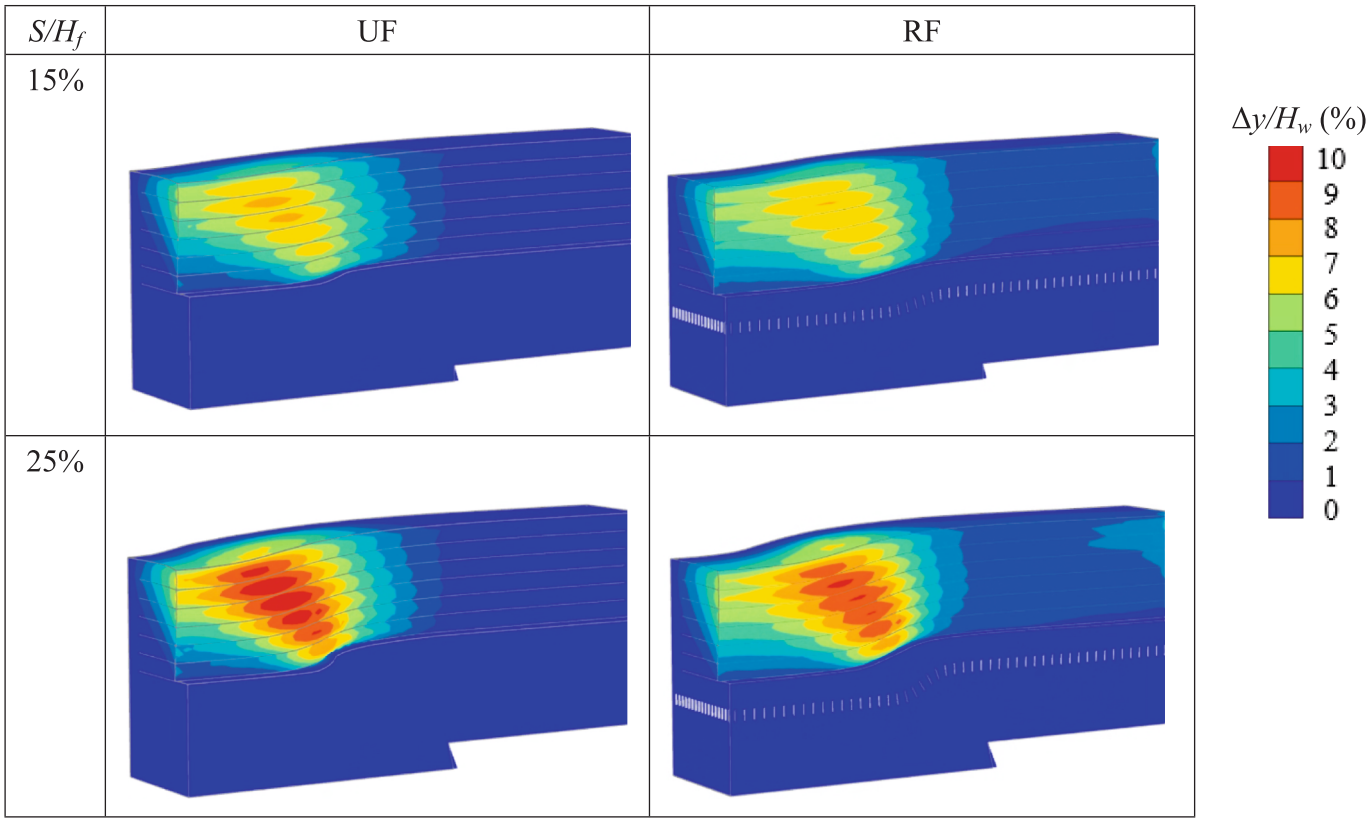

Fig. 16. Contours of normalized embankment facing displacement.

fault displacements. The numerical models were first validated against experimental results, after which they were used to evaluate the mechanical behavior of the GRS embankment and foundation system. The main findings of this study are summarized as follows:

- The NS model outperformed the HS model by accurately reproducing post-peak strain-softening, shear band propagation, and embankment facing displacement under reverse faulting. In contrast, the HS model underestimated the embankment facing displacement and failed to capture the bending of the shear band in the unreinforced foundation.
- Two reinforcing mechanisms of the geocell foundation, shear band interception and bending resistance, were identified. The geocell mattress provided additional confinement to the infill soil, which consequently increased soil shear strength and intercepted the fault-induced shear band. The bending stiffness of the geocell mattress resisted compressive forces induced by reverse fault movement, thereby dissipating the stress transmitted to the embankment.
- Incorporating the geocell mattress into the foundation reduced the maximum σ'_{yy} within the retained zone and substantially decreased the facing displacement of the overlying embankment. These

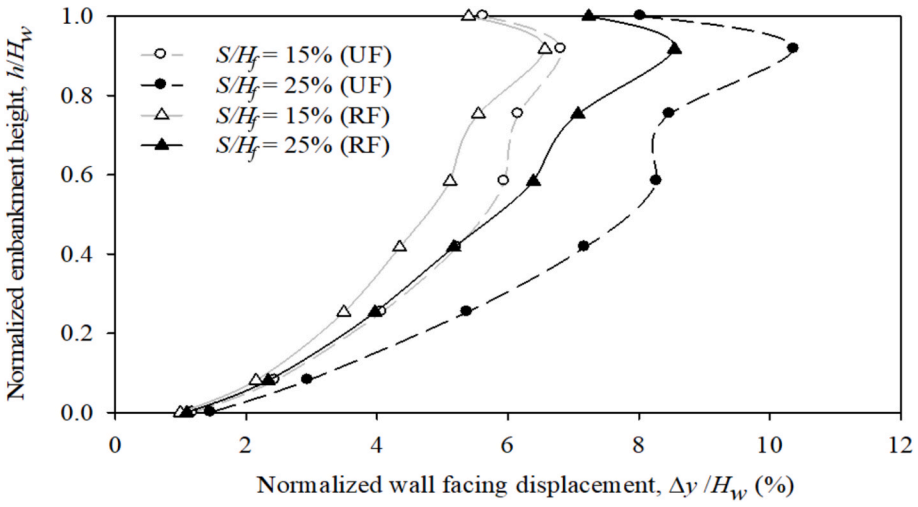

Fig. 17. Profiles of $\Delta y/H_w$ with normalized embankment heights.

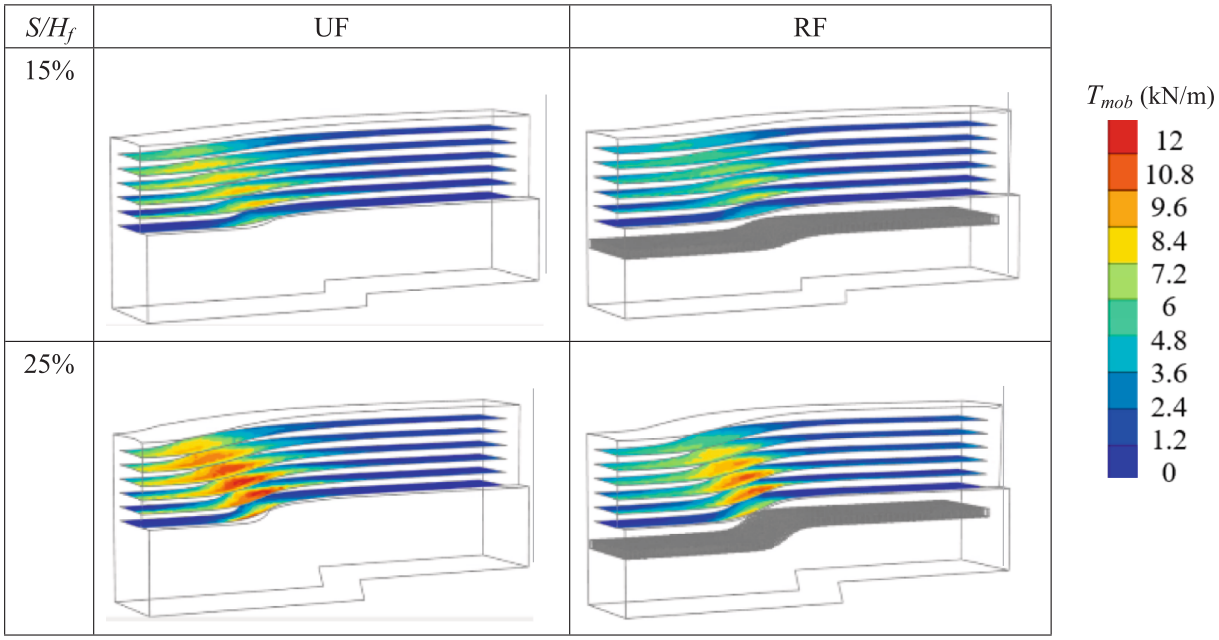

Fig. 18. Contours of mobilized tensile forces in the embankment's reinforcement layers in the transverse direction.

improvements demonstrate the vital role of geocell foundations in enhancing embankment stability, particularly at large fault offsets.

- The T_{mob} in the reinforcement layers of the embankment in the transverse direction increased with fault offsets, with T_{max} occurring at the location intersecting with the shear band. In the RF case, the envelope of T_{max} was displaced away from the Rankine active failure plane, indicating an increase in effective reinforcement length and embankment stability.
- The GRS embankment overlying the geocell foundation exhibited a reduced $\Delta y/H_w$ value approaching the lower bound of the limit state for GRS walls under strong earthquakes, thereby maintaining overall stability despite localized deformation, which can be readily repaired after an earthquake to restore highway serviceability.

Although this study primarily examined the response of GRS embankment and foundation systems to reverse fault movement, the influence of seismic loading, fault dip angle, and the design parameters of geocell foundations on the system's performance were not evaluated. These factors should be investigated in future research to better understand the underlying mechanisms and improve design approaches for mitigating surface fault hazards.

CRediT authorship contribution statement

Jung Chiang: Writing – review & editing, Visualization, Validation, Methodology, Investigation, Data curation. **Emerson Edwige Michel:** Writing – original draft, Visualization, Methodology, Investigation, Formal analysis, Data curation. **Kuo-Hsin Yang:** Writing – review & editing, Visualization, Supervision, Resources, Methodology, Investigation, Funding acquisition, Data curation, Conceptualization.

Declaration of competing interest

The authors declare that they have no known competing financial interests or personal relationships that could have appeared to influence the work reported in this paper.

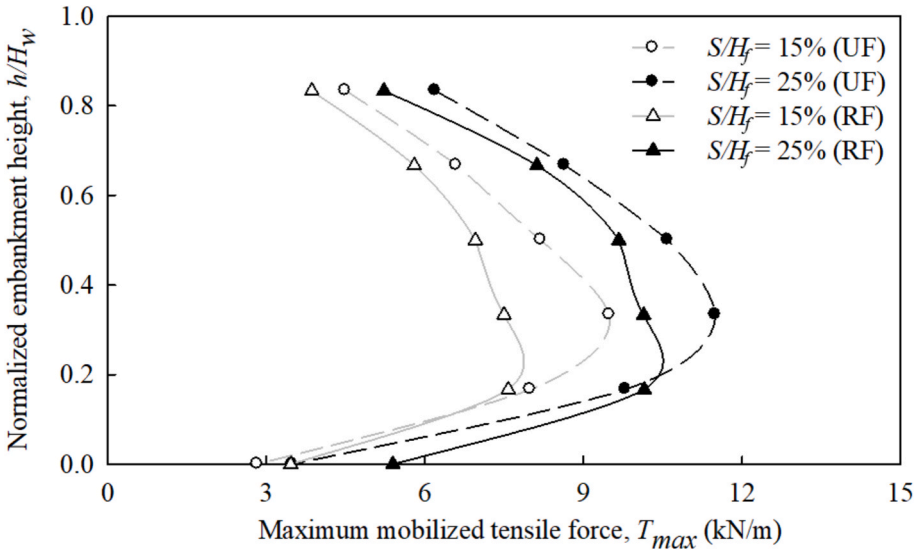

Fig. 19. Profiles of the maximum mobilized tensile forces with normalized embankment heights.

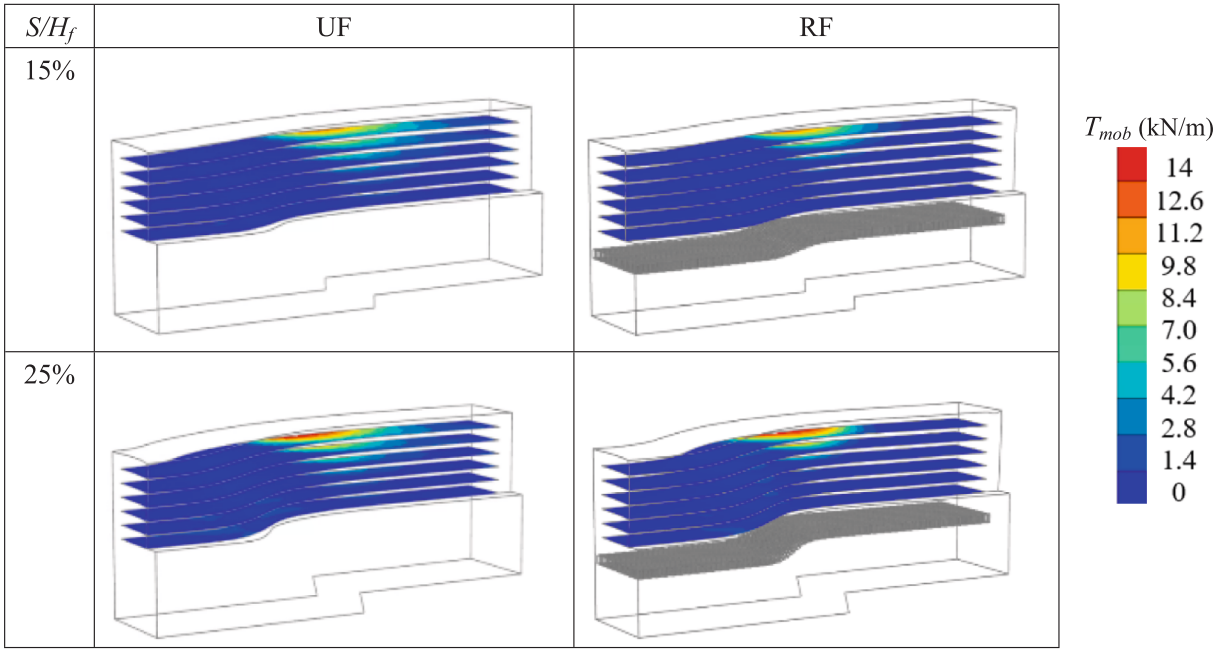

Fig. 20. Contours of mobilized tensile forces in the embankment's reinforcement layers in the longitudinal direction.

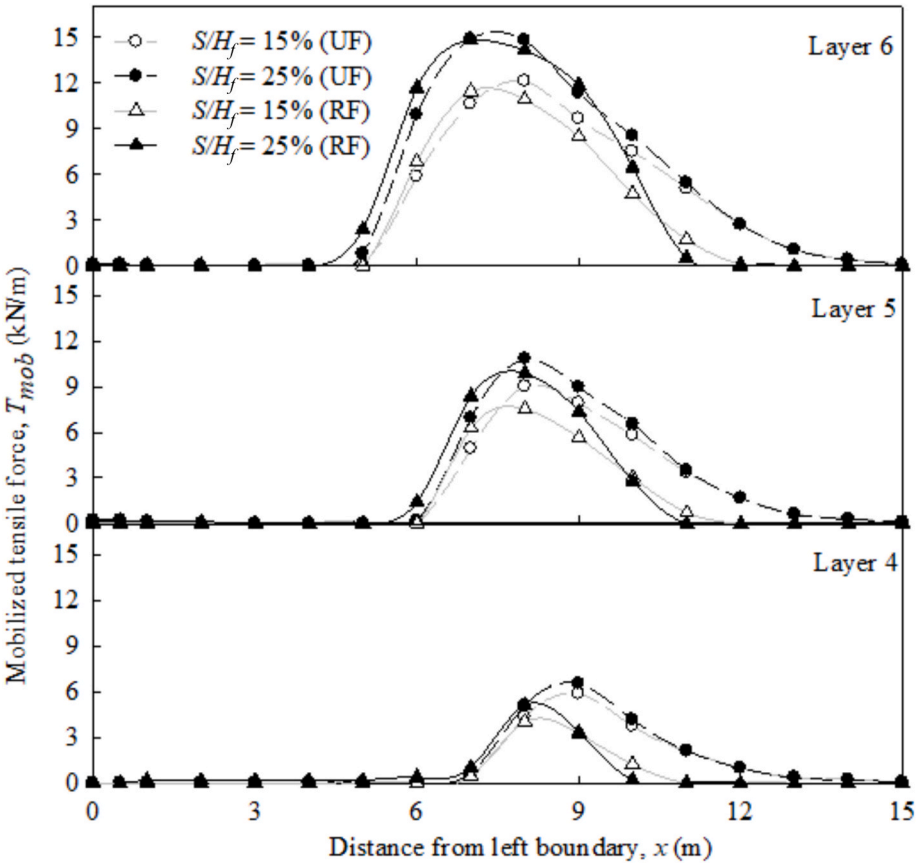

Fig. 21. Distribution of mobilized tensile forces in the embankment's reinforcement layers in the longitudinal direction.

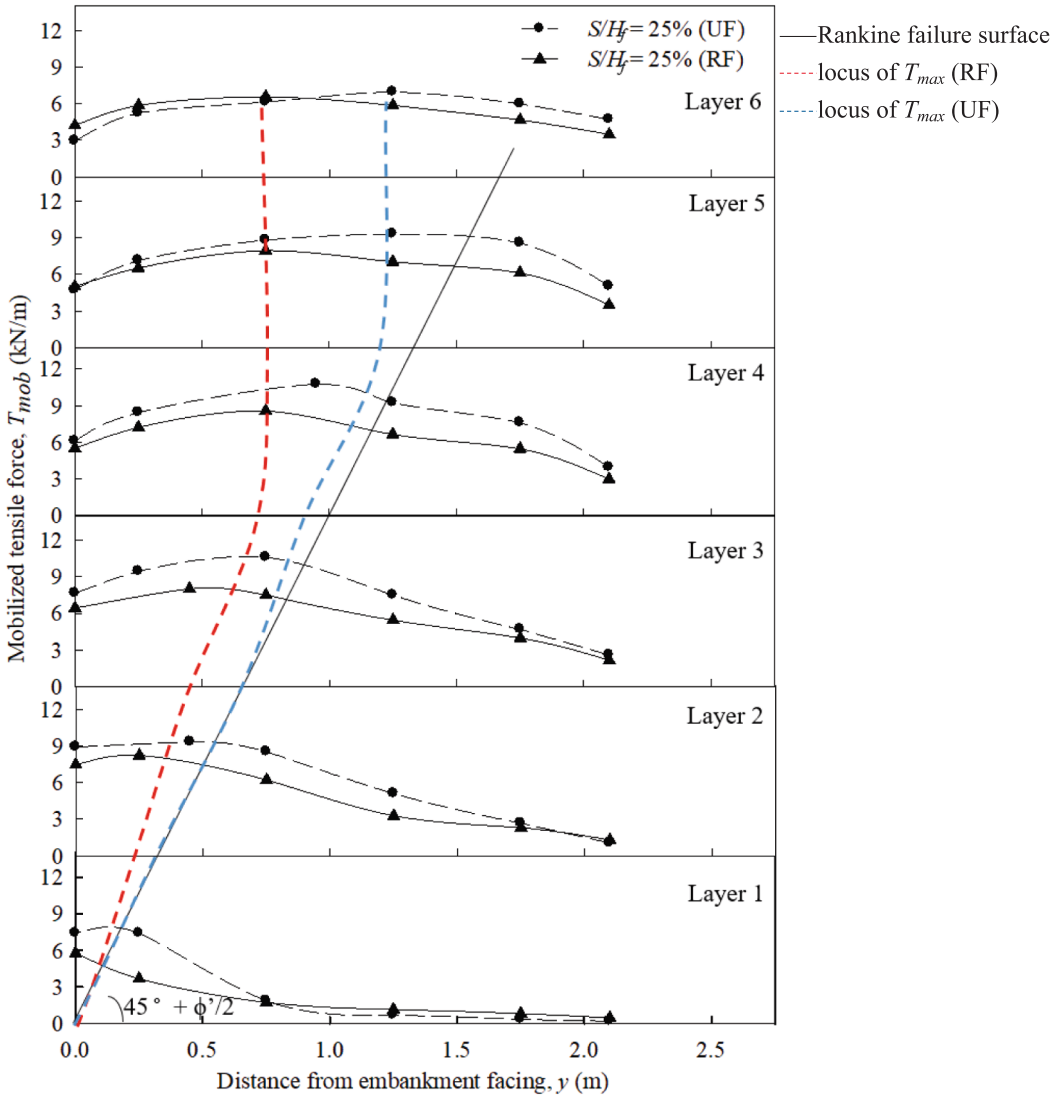

Fig. 22. Loci of maximum reinforcement tensile forces near outcrop at S/H_f = 25%.

Acknowledgement

This study was motivated by a construction project featuring a GRS structure built across the Chelungpu Fault in Central Taiwan. The authors sincerely show deep gratitude to Sinotech Engineering Consultants for providing detailed information on the project's design and construction. This research was supported by the National Science and Technology Council of Taiwan under grant numbers MOST 110-2628-E-002-003 and NSTC 112-2811-E-002-001.

Data availability

Data will be made available on request.

References

[1] AASHTO LRFD Bridge Design Specifications. 6th ed. Washington, D.C., U.S.A. American Association of State Highway and Transportation Officials; 2012.
[2] Ahmadi N, Fadaee M. Mechanical behavior of soil foundations reinforced with geosynthetics exposed to normal and reverse fault ruptures. Period Polytech, Civ Eng 2023;67(1):123–40.
[3] Anastasopoulos I, Gazetas G, Bransby MF, Davies MC, El Nahas A. Normal fault rupture interaction with strip foundations. J Geotech Geoenviron Eng ASCE 2009; 135(3):359–70.
[4] Ashtiani M, Ghalandarzadeh A, Mahdavi M, Hedayati M. Centrifuge modeling of geotechnical mitigation measures for shallow foundations subjected to reverse faulting. Can Geotech J 2017;55(8):1130–43.
[5] Been K, Jefferies MG, Hachey J. The critical state of sand Géotechnique 1991;41 (3):365–81.
[6] Bolarinwa A, Kalatehjari R, Rashid ASA. Critical state characterization of New Zealand East Coast sand for numerical modeling. Geotech Geol Eng 2023;42(5): 1239–57.
[7] Bonilla MG. Historic surface faulting in the continental United States and adjacent parts of Mexico. US Geological Survey 1967:TID–24124.
[8] Bray JD. Earthquake surface fault rupture design considerations. Proceedings of the Sixth International Conference on Urban Earthquake Engineering. Tokyo, Japan; 2009.
[9] Bray JD. Developing mitigation measures for the hazards associated with earthquake surface fault rupture. A Workshop on Seismic Fault-Induced failures – possible Remedies for damage to Urban Facilities. Japan: Japan Society for Promotion of Science, University of Tokyo; 2001.
[10] Bray JD, Ashmawy A, Mukhopadhyay G, Gath EM. Use of geosynthetics to mitigate earthquake fault rupture propagation through compacted fill. Proceedings of the Geosynthetics '93 Conference. Vancouver, Canada; 1993.
[11] Bray JD, Seed RB, Cluff LS, Seed HB. Earthquake fault rupture propagation through soil. J Geotech Eng ASCE 1994;120(3):543–61.
[12] Brinkgreve RBJ, Kumarswamy S, Swolfs WM, Zampich L, Ragi Manoj N. PLAXIS 3D manualBentley Systems Inc. NetherlandsPLAXIS B.V 2019.
[13] Buckingham E. On physically similar systems: Illustrations of the use of dimensional equations. Phys Rev 1914;4(4):345–76.
[14] Chiang J, Wu C-W, Yang K-H, Chung Y-C, Viswanadham BVS. Performance of various geosynthetic-reinforced embankment and foundation systems subjected to reverse fault movement. J Geotech Geoenviron Eng ASCE 2025;151(4):04025018.

[15] Chiang J, Michel EE, Yang K-H, Zornberg JG. Mitigation of reverse faulting in foundation soils using geosynthetic-encased granular columns. Transp Geotech 2023;42:101067.
[16] Chiang J, Yang K-H, Chan Y-S, Yuan C-L. Finite element analysis and design method of geosynthetic-reinforced soil foundation subjected to normal fault movement. Comput Geotech 2021;139:104412.
[17] da Fonseca AV, Cordeiro D, Molina-Gómez F. Recommended procedures to assess critical state locus from triaxial tests in cohesionless remoulded samples. Geotechnics 2021;1(1):95–127.
[18] Faccioli E, Anastasopoulos I, Gazetas G, Callerio A, Paolucci R. Fault rupture–foundation interaction: selected case histories. Bull Earthq Eng 2008;6(4):557–83.
[19] Fadaee M, Ezzatyazdi P, Anastasopoulos I, Gazetas G. Mitigation of reverse faulting deformation using a soil bentonite wall: dimensional analysis, parametric study, design implications. Soil Dyn Earthq Eng 2016;89:248–61.
[20] Faria AO, Junior MPS, Carneiro JJV, Pinto GHS, Dias MVL. Evaluation of the susceptibility to flow liquefaction of an iron ore tailings using the state parameter and yield stress ratio approach. Proceedings of the 7th International Conference on Geotechnical and Geophysical Site Characterization. Barcelona, Spain; 2024.
[21] Fuentes EC, Zdravković L, Potts DM. On the calibration and application of the NorSand model. Proceedings of the 10th European Conference on Numerical Methods in Geotechnical Engineering, London, UK; 2023.
[22] Garcia FE, Bray JD. Discrete-element analysis of influence of granular soil density on earthquake surface fault rupture interaction with rigid foundations. J Geotech Geoenviron Eng ASCE 2019;145(11):04019093.
[23] Garcia FE, Bray JD. Discrete element analysis of earthquake fault rupture–soil–foundation interaction. J Geotech Geoenviron Eng ASCE 2019;145(9):04019046.
[24] Garcia FE, Gallage CPK, Uchimura T. Function of permeable geosynthetics in unsaturated embankments subjected to rainfall infiltration. Geosynth Int 2007;14(2):89–99.
[25] Gazetas G, Pecker A, Faccioli E, Paolucci R, Anastasopoulos I. Preliminary design recommendations for dip-slip fault–foundation interaction. Bull Earthq Eng 2008;6(4):677–87.
[26] Hung W-Y, Yang K-H, Nguyen TS, Pham TNP. Performance of geosynthetic-reinforced soil walls at failure. J GeoEng 2020;15(1):13–29.
[27] Jefferies MG. NorSand: a simple critical state model for sand. Géotechnique 1993;43(1):91–103.
[28] Jefferies MG, Been K. Soil liquefaction: a critical state approach. Applied Geotechnics Series. CRC Press, Taylor and Francis; 2015.
[29] Jefferies MG, Shuttle DA. NorSand: Features, calibration and use. ASCE, Austin, Texas: Geo-Frontiers Congress; 2005.
[30] Jefferies MG, Shuttle DA. Dilatancy in general Cambridge-type models. Géotechnique 2002;52(9):625–38.
[31] Khorsandiardebili N, Ghazavi M. Static stability analysis of geocell-reinforced slopes. Geotext Geomembr 2021;49(3):852–63.
[32] Lazarte CA, Bray JD. A study of strike-slip faulting using small-scale models. Geotech Test J 1996;19(2):118–29.
[33] Lazarte CA, Bray JD, Johnson AM, Lemmer RE. Surface breakage of the 1992 Landers earthquake and its effects on structures. Bull Seismol Soc Am 1994;84(3):547–61.
[34] Lin M-L, Chung C-F, Jeng F-S. Deformation of overburden soil induced by thrust fault slip. Eng Geol 2006;88(1–2):70–89.
[35] Loli L, Kourkoulis R, Gazetas G. Physical and numerical modeling of hybrid foundations to mitigate seismic fault rupture effects. J Geotech Geoenviron Eng ASCE 2018;144(11):04018083.
[36] Mehdipour I, Ghazavi M, Moayed RZ. Numerical study on stability analysis of geocell reinforced slopes by considering the bending effect. Geotext Geomembr 2013;37(1):23–34.
[37] Nowkandeh MJ, Ashtiani M. A novel mitigation measure for normal fault-induced deformations on pile-raft systems. Earthq Eng Eng Vib 2024;23(1):15–33.
[38] Oettle NK, Bray JD. Geotechnical mitigation strategies for earthquake surface fault rupture. J Geotech Geoenviron Eng ASCE 2013;139(11):1864–74.
[39] Pokharel SK, Han J, Leshchinsky D, Parsons RL, Halahmi I. Investigation of factors influencing behavior of single geocell-reinforced bases under static loading. Geotext Geomembr 2010;28(6):570–8.
[40] Rasouli H, Fatahi B. Geosynthetics reinforced interposed layer to protect structures on deep foundations against strike-slip fault rupture. Geotext Geomembr 2021;49(3):722–36.
[41] Rivas NA, Sottile MG, López Rivarola F, Sfriso AO. Comparing HSS and NorSand constitutive models for modelling flow liquefaction in tailings dams. Brazil: Ouro Preto; 2023.
[42] Schanz T, Vermeer PA, Bonnier PG. Formulation and verification of the Hardening-Soil Model. Proceedings of the Beyond 2000 in Computational Geotechnics Conference. Amsterdam, Netherlands; 1999.
[43] Tang X, Yang M. Investigation of flexural behavior of geocell reinforcement using three-layered beam model testing. Geotech Geol Eng 2013;31(2):753–65.
[44] Viswanadham BVS, Konig D. Studies on scaling and instrumentation of a geogrid. Geotext Geomembr 2004;22(5):307–28.
[45] Woudstra LJ. Verification, Validation and Application of the NorSand Constitutive Modeling in PLAXIS. Delft University of Technology; 2021.
[46] Yang K-H, Chiang J, Lai C-W, Han J, Lin M-L. Performance of geosynthetic-reinforced soil foundation across a normal fault. Geotext Geomembr 2020;48(3):357–73.
[47] Yasuhara K, Recio-Molina J. Geosynthetic-wrap around revetments for shore protection. Geotext Geomembr 2007;25(4–5):221–32.
[48] Yoo C, Tabish A, Yang JW, Abbas Q, Song JS. Effect of internal drainage on deformation behavior of GRS wall during rainfall. Geosynth Int 2022;29(2):137–50.
[49] Zhang L, Ou Q, Zhao M. Double-beam model to analyze the performance of a pavement structure on geocell-reinforced embankment. J. Eng. Mech., ASCE 2018;4(8):06018002.